Impact of Aerosol Intrusions on Arctic Boundary Layer Clouds. Part II: Sea Ice Melting Rates

G. G. CARRIÓ, H. JIANG, AND W. R. COTTON

Department of Atmospheric Science, Colorado State University, Fort Collins, Colorado

(Manuscript received 30 October 2003, in final form 28 July 2004)

ABSTRACT

The potential impact of intrusions of polluted air into the Arctic basin on sea ice melting rates and the surface energy budget is examined. This paper extends a previous study to cloud-resolving simulations of the entire spring season during the 1998 Surface Heat Budget of the Arctic (SHEBA) field campaign. For that purpose, the Los Alamos National Laboratory sea ice model is implemented into the research and real-time versions of the Regional Atmospheric Modeling System at Colorado State University (RAMS@CSU). This new version of RAMS@CSU also includes a new microphysical module that considers the explicit nucleation of cloud droplets and a bimodal representation of their spectrum. Different aerosol profiles based on 4 May 1998 observations were used to characterize the polluted upper layer and the 2–3 daily SHEBA soundings were utilized to provide time-evolving boundary conditions to the model. Results indicate that entrainment of ice-forming nuclei (IFN) from above the inversion increases the sea ice melting rates when mixed-phase clouds are present. An opposite although less important effect is associated with cloud condensation nuclei (CCN) entrainment when liquid-phase clouds prevail.

1. Introduction

Changes in the Arctic sea ice could potentially alter global climate via changes in the thermohaline circulation and the location of storm tracks (Royer et al. 1990; Alexander et al. 2004). The presence or absence of clouds has a large impact on this critical component of the climate system that strongly influences albedo, and the surface heat and momentum fluxes (Maykut and Understeiner 1971). In particular, low-level cloudiness exerts a strong influence on the surface energy budget over the Arctic basin (Curry et al. 2000; Perovich et al. 1999). Therefore, Arctic clouds have been the object of numerous studies because of the growing awareness of the sensitivity of the Arctic climate to global warming (for a review see Curry et al. 1996). From the perspective of global climate models, Gregory and Morris (1996) have emphasized the impact of bulk cloud properties on the energy balance and the stability of sea ice. On the other hand, several authors have discussed the possible role that atmospheric aerosols play by changing cloud optical properties (Shaw 1986; Heintzenberg et al. 1986; Curry and Ebert 1990, 1992). Increased concentrations of cloud condensation nuclei (CCN) may reduce the cloud droplet effective radius, and increase cloud reflectivity, cloud droplet number concentration and downward longwave radiation at the surface. Enhanced concentrations of ice-forming nuclei (IFN) would affect the phase of the condensed water and also increase the ice particle concentration. In the case of Arctic mixed-phase boundary layer clouds, the evolution, the thermodynamics, and the cloud-scale dynamics are intimately tied to the microphysics. Therefore, net aerosol effects cannot be numerically examined correctly unless the model is capable of taking into account these complex interactions and explicitly resolving the bulk turbulent field. In that regard, several authors performed cloud-resolving and large eddy simulations (LES) of Arctic boundary layer clouds, revealing that these cloud systems are quite vulnerable to rather modest changes in CCN and IFN concentrations (Olsson et al. 1998; Harrington et al. 1999; Olsson and Harrington 2000; Jiang et al. 2000, 2001; Carrió et al. 2005).

During the recent First International Satellite Cloud Climatology Project (ISCCP) Regional Experiment/ Surface Heat Budget of the Arctic Ocean (FIRE/

Corresponding author address: Gustavo Gabriel Carrió, Atmospheric Science Building, Office 225, Colorado State University, Fort Collins, CO 80523.
E-mail: carrio@atmos.colostate.edu

SHEBA) spring field campaign intensive operation period (IOP), the air mass was found to be moderately polluted in terms of CCN and IFN above the boundary layer and extremely clean below on several occasions (Rogers et al. 2001; Curry et al. 2000; Jiang et al. 2001). The term polluted is used in this paper to describe enhanced IFN and/or CCN concentrations without implying that the origin of these aerosols is necessarily anthropogenic. Jiang et al. (2001) conducted two sets of three-dimensional simulations of a springtime Arctic boundary layer cloud observed during the FIRE/SHEBA 1998 on 18 May 1998 to study the influence of entrainment of CCN at cloud top on the cloud microphysical and dynamical structure, radiative properties, and cloud evolution. The above-mentioned study was run with explicit representation of the CCN spectrum and cloud droplet spectrum (Feingold et al. 1994). The initial CCN concentration in the base run was a constant value of 30 cm^{-3} (activated at 0.8% supersaturation). The CCN concentration in the sensitivity run varied from 30 cm^{-3} below cloud base to a peak of 250 cm^{-3} at the inversion, which was similar to the observed values (Yum and Hudson 2001). Results in the sensitivity run showed that droplet concentrations were about twofold higher than the base run and effective radii are 9% to 15% lower from cloud top to cloud base, respectively. Furthermore, liquid water content was 21% higher compared to the base run, and no drizzle reached the ground in the sensitivity run. There were also differences in the dynamics as the sensitivity run had more vigorous eddies especially at the end of 5-h simulation. Differences in cloud optical properties were apparent right from the beginning of the simulations. The sensitivity run showed 12% higher cloud albedo and 33% greater cloud optical depth. These results were consistent with both observations and modeling studies. Unfortunately the case studied by Jiang et al. (2001) was too warm to examine the impact of entrained IFN on the cloudy boundary layer.

Carrió et al. (2005, hereafter referred to as Part I) performed a series of sensitivity numerical experiments for the 4 May 1998 mixed-phase case (SHEBA/FIRE) by modifying the initial IFN/CCN profiles above the top of the boundary layer. In the control run we assumed a constant clean profile ($\sim 4\ L^{-1}$) and in all other simulations we considered the observed polluted profile multiplied by factors between 1/3 and 2 above the inversion (and a clean profile below). All simulations were performed using the two-moment microphysical treatment that predicts mixing ratios and number concentrations for all hydrometeors. Results demonstrated a significant impact of IFN entrainment from above the inversion on the microstructure of the simulated clouds. The observed secondary ice water content (IWC) maximum just below the inversion could only be produced in the model by assuming the observed polluted initial IFN profiles. The liquid water fraction of the cloud monotonically decreased when more polluted initial IFN profiles were assumed. Droplets located near the top of the boundary layer were the most affected, with their concentrations and mean diameters lower than the control run. The significant increase in the ice water path resulted in higher total condensate paths as well as higher downward longwave fluxes.

It should be pointed out that we previously performed case studies of sensitivity of Arctic clouds to simple change in IFN from an idealized case (Harrington et al. 1999) to a real case (Jiang et al. 2000) of a mixed-phase Arctic clouds during the fall transition. We conducted the three-month simulations in this study as a continuation of our previous work with emphasis on the impact of changing IFN/CCN on sea ice melting during spring transition season, as we anticipate some of the major results of Jiang et al. (2000) will be reproduced.

The present paper examines the potential impact of intrusions of polluted air into the Arctic basin on sea ice melting rates and the surface energy budget. We present a series of sensitivity numerical experiments performed with a two-dimensional fine resolution version of the Regional Atmospheric Modeling System at Colorado State University (RAMS@CSU) coupled with the Los Alamos National Laboratory sea ice model (CICE; Hunke and Lipscomb 1999). Different aerosol concentrations were assumed to characterize the polluted upper layer and the 2–3 daily SHEBA soundings were used to provide time-evolving boundary conditions to these cloud-resolving simulations.

A brief description of the new model is given in section 2. Section 3 considers the design of the numerical sensitivity experiments and general simulation conditions. Results, and summary and conclusions are presented in sections 4 and 5, respectively.

2. Model description

The model used in this study is the two-dimensional (2D) cloud-resolving model version of RAMS developed at Colorado State University (Pielke et al. 1992; Cotton et al. 2003). Simulations were performed with the same microphysical treatment used in Part I. This new microphysical package (Saleeby and Cotton 2004) shares the double-moment microphysical framework of the previous scheme (Meyers et al. 1997), which assumes that hydrometeor size spectra have a gamma distribution function and mass mixing ratio as well as num-

ber concentration of the hydrometeor species. However, among the new features it explicitly considers the nucleation of cloud droplets via activation of CCN concentration, a bimodal representation of the cloud droplet spectrum, and prediction of mixing ratios and concentrations for both modes. The predicted microphysical categories also include the number concentration and mixing ratio of rain, pristine ice, snow, aggregates, graupel, and hail, as well as the IFN and CCN concentrations. IFN can be defined as a vertically and/or horizontally heterogeneous variable that can be advected and diffused (Cotton et al. 2003). Snow is defined as larger pristine ice crystals (>100 μm), which grow by vapor deposition and riming while aggregates are defined as ice particles formed by collision and coalescence of pristine ice, snow or other aggregates. A more detailed description of the microphysics treatment was given in Part I.

The two-stream radiative model utilized for this study (Harrington et al. 1999) solves the equation of transfer for three gaseous constituents H_2O, O_3, and CO_2, which include climatological mixing ratios of CH_4, O_2, and NO_2. Gaseous absorption is calculated by following the fast exponential sum-fitting transmission method proposed by Ritter and Geleyn (1992). Lorenz–Mie theory is used to compute the optical properties for cloud droplets, while the theory of Mitchell et al. (1996) is used for nonspherical ice crystals. For each hydrometeor species, the band-averaged values of optical properties are computed for the assumed gamma distribution used in RAMS following the method of Slingo and Schreckner (1982).

The CICE model (Hunke and Lipscomb 1999) has been interfaced with the research and real-time versions of RAMS@CSU. This sea ice model discretizes the subgrid ice thickness distributions in different thickness categories, considering their corresponding fractional areas as prognostic variables. The CICE treatment of the ice thermodynamics is very similar to that of Maykut and Untersteiner (1971). Ice thickness categories are partitioned in a number of internal ice layers. For each thickness category, the surface and snow temperatures as well as the temperatures associated with the internal layer are also prognostic variables. However, salinity and density profiles are prescribed. Heat capacity, thermal conductivity, and enthalpy of sea ice are considered dependent on both temperature and salinity.

The original version of CICE was modified in its structure to allow module communication in an interactive multigrid framework. Routines have been included to evaluate the surface momentum fluxes corresponding to each thickness category (and open sea), and various improvements have been made to provide more realistic turbulent surface fluxes and albedo over Arctic interior ice regions. Iterative methods that consider variable roughness lengths have been applied to evaluate momentum and heat fluxes. The saltation of snow was considered to evaluate the roughness lengths independently for each thickness category with nonnegligible snow cover. For the purpose of real-time forecasting, this new coupled version of RAMS@CSU can automatically process the National Aeronautics and Space Administration (NASA) Special Sensor Microwave Imager (SSM/I) F13 25-km sea ice coverage data. The data are objectively analyzed and mapped to the model grid configuration.

For this study, six ice thickness categories (with four internal layers) were considered to describe the subgrid-scale ice thickness distribution of each horizontal grid cell. The mass and energy-conserving remapping scheme of Lipscomb (2001) was used to transfer ice among categories. Because of the small horizontal dimension of the cloud-resolving model, the changes in thickness distribution associated with dynamic processes (i.e., ridging and ice shear) were taken into account using the SHEBA daily time series of divergence and shear rates. All simulations were initialized with an ice thickness and snow depth of 2.41 and 0.23 m, respectively. These values approximately correspond to the average values of the seven gauges closest to the SHEBA site for 1 May 1998.

3. Experiment design and model grid structure

This series of cloud-resolving model (CRM) simulations places special emphasis on examining the impact of IFN/CCN entrainment from above the inversion on sea ice melting rates and the surface energy budget. The general structure of the numerical sensitivity experiments is very similar to that of Part I (4 May 1998 case), in that observed IFN and CCN vertical profiles multiplied by different factors were assumed for initialization of aerosol concentration above the boundary layer. Moreover, aerosol data from this Arctic boundary layer cloud observed during FIRE/SHEBA field experiment, were used to characterize the polluted air layer overriding the inversion for these multimonth simulations. The CCN data collected during FIRE-Arctic Cloud Experiment (ACE) project using instantaneous CCN Spectrometer of Desert Research Institute (DRI) indicate concentrations of approximately 100 and 250 cm^{-3} (active at 1% supersaturation) for below and above the inversion, respectively (Yum and Hudson 2001). The IFN vertical profile derived from the CSU continuous

TABLE 1. Description of experiments.

Experiment	IFN	CCN
EC-C (control run)	Clean	Clean
EC-1	Clean	Observed
E.50-C	1/2 × observed	Clean
E.50–1	1/2 × observed	Observed
E.75–1	3/4 × observed	Observed
E1-C	Observed	Clean
E1–1	Observed	Observed

flow diffusion chamber (CDFD) Ice Nucleus Counter data, exhibits relatively large concentrations above the boundary layer with a maximum value of 85.6 L^{-1}, while below the inversion the vertical average is approximately 3 L^{-1} (Rogers et al. 2001).

The simulations were initialized using different IFN and CCN profiles based on those observed above the boundary layer. Conversely, the initialization profiles for all experiments assume clean concentrations of IFN and CCN (3 L^{-1} and 100 cm^{-3}, respectively) within the boundary layer. Only the initialization profiles corresponding to the control run assume clean IFN profiles for both layers. Both IFN and CCN concentrations were defined as horizontally heterogeneous variables that vary because of advection, diffusion, activation, and evaporation/sublimation of cloud particles. To isolate the effect of the entrained aerosols efficiently, a Newtonian relaxation technique (nudging) was applied to restore the polluted and clean aerosol concentrations above and below the current altitude of the inversion, respectively. For this reason, the initialization profiles associated with the observations (hereafter referred to as observed) were defined as a vertical average of the observed aerosol profiles within the upper layer, instead of retaining their vertical structure as done in Part I. A summary of multimonth CRM runs that correspond to the results presented in this paper is given in Table 1.

All the experiments have been performed in a two-dimensional (2D) framework. The simulation domain was 5000 m in the horizontal and approximately 3325 m in the vertical. A constant horizontal grid spacing of 50 m and a time step of 2 s were used. The vertical grid was stretched using the relationship $\Delta z_{k+1} = 1.05\ \Delta z_k$ with 30 m spacing at the finest to provide a better resolution within the boundary layer. The lateral boundary conditions were cyclic and the domain top is a rigid lid. Rayleigh damping was used in the five highest levels of the domain to prevent the reflection of vertically traveling gravity waves off this rigid lid. Noninertial effects were neglected.

Because of the small dimensions of the domain, horizontally homogeneous initialization was chosen. The 2–3 daily SHEBA soundings were used to take into account large-scale forcing during the 92-day period. Special care was taken to provide time-evolving boundary conditions to the model without affecting the fine-scale features developed into the CRM domain. Nudging in this study takes the following form:

$$\Psi(k, i, t) = \Psi(k, i, t - \Delta t) + \text{model} + [\Psi^{\text{obs}}(k) - \Psi^{\text{H}}(k, t - \Delta t)]/\tau, \quad (1)$$

where $\Psi(k, i, t)$ is the predicted value of a nudged variable Ψ at the end of the current time step, $\Psi(k, i, t - \Delta t)$ is the model Ψ value at the end of the previous time step, model includes advection, diffusion, thermodynamic/microphysical effects, etc.; Ψ^{obs} is the vertical profile being nudged to and is a function of the vertical index k, $\Psi^{\text{H}}(k, t - \Delta t)$ is the horizontal average of Ψ at the end of the previous time step, and τ denotes the relaxation time.

Using Ψ^{H} instead of Ψ avoids nudging out the fine-scale features developed in the CRM. The values of Ψ^{obs} used to nudge the horizontal wind component, total mixing ratio, potential temperature were evaluated from SHEBA soundings by using a linear interpolation method and a value of 12 h was assumed for τ. As mentioned above, nudging of IFN and CCN concentrations was considered to restore initialization values within and above the boundary layer. Therefore, aerosol nudging profiles (Ψ^{obs}) were defined as step functions with the discontinuity that varies in time according to the current altitude of the inversion. A value of 48 h was assumed for τ when nudging of IFN and CCN concentrations.

4. Results

We generated probability density functions (PDFs) of various variables for the entire 3-month period in order to establish comparisons between numerical experiments as well as between some simulated and observed radiative fluxes. Figure 1 shows the PDFs of the short- and longwave downwelling fluxes at the surface (SWDN and LWDN, respectively) obtained for experiment control run (EC-C) and for the observations. For both surface fluxes, the curves corresponding to simulated and observed data exhibit very similar patterns and the positions of the modes are almost coincident. However, the magnitude of the LWDN mode associated with the observations is larger while the PDF of simulated values is wider. Differences between the PDFs of SWDN indicate that large values tend to be slightly more frequent for the control run. PDFs for simulated and observed values of the longwave up-

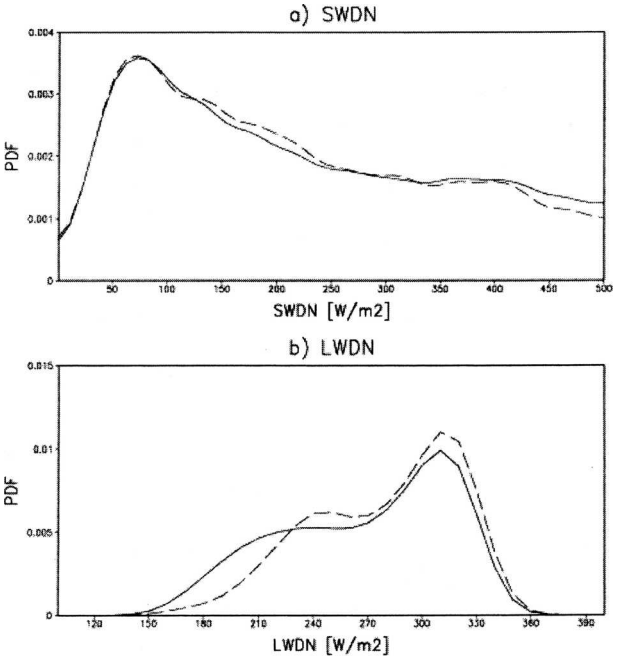

FIG. 1. (a) Probability density functions of observed and simulated longwave downwelling flux at the surface (LWDN). (b) Probability density functions of observed and simulated shortwave downwelling flux at the surface (SWDN). Dashed and solid lines denote observed and simulated values, respectively.

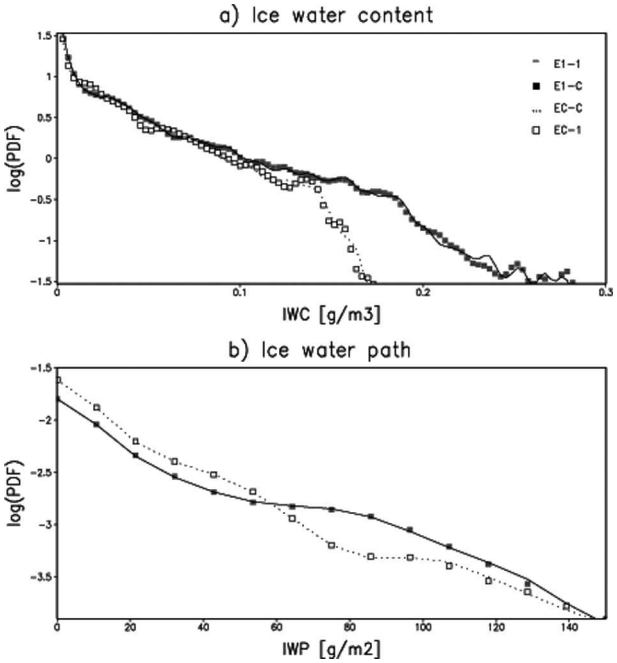

FIG. 2. Probability density functions of (a) IWC and (b) IWP for runs EC-1, EC-C, E1-1, and E1-C.

welling flux at the surface are virtually identical (not shown). The differences between the PDFs of the observed and simulated LWDN and SWDN may be explained by the presence of upper-layer clouds at times. The model domain was less than 4000 m deep and the vertical grid was stretched in the vertical to provide a better resolution within the boundary layer, the main focus of this study. However, this grid setup imposes a limitation in simulating the radiative contribution of upper-layer clouds.

We also generated probability density functions of various microphysical variables associated with ice-phase cloud particles. Figure 2 compares the PDFs of ice water content and ice water path (IWP), for experiments EC-C, EC-1, E1-C, and E1-1. These curves consist of hourly averaged values corresponding to each grid cell (IWC) and each vertical column (IWP) of the domain. These two quantities represent all solid ice (i.e., pristine ice, snow, and aggregates). On the one hand, substantial differences can be observed between runs that consider enhanced IFN concentrations above the boundary layer (E1-C and E1-1) compared to those where clean IFN profiles (EC-C and EC-1) are assumed. Large IWC and IWP values are more frequent for the run that assumed enhanced IFN concentrations (E1-C and E1-1). On the other hand, for the same IFN simulation conditions, the curves do not significantly differ whether enhanced CCN concentrations or clean profiles were assumed within the upper layer.

Figure 3a gives the PDFs of total number concentra-

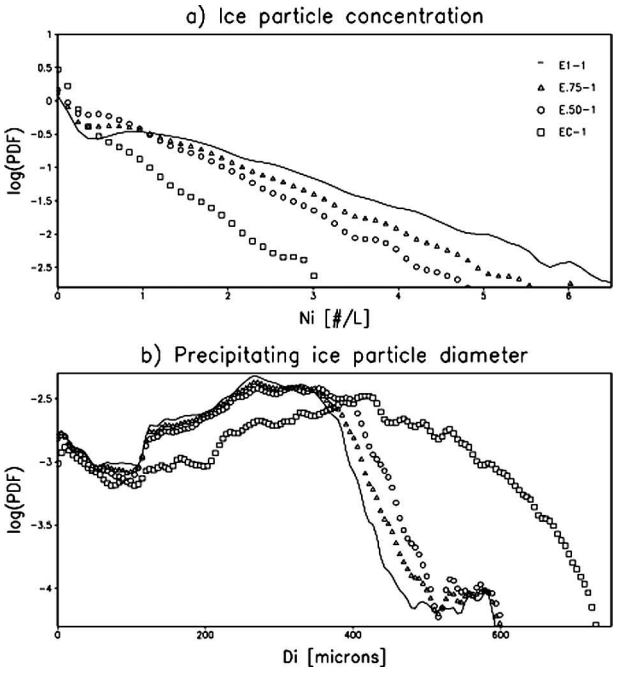

FIG. 3. Probability density functions of the ice particle number concentration (N_i) and mean mass diameter of precipitating ice particles (D_i) for experiments EC-1, E.50-1, E.75-l, and E1-1.

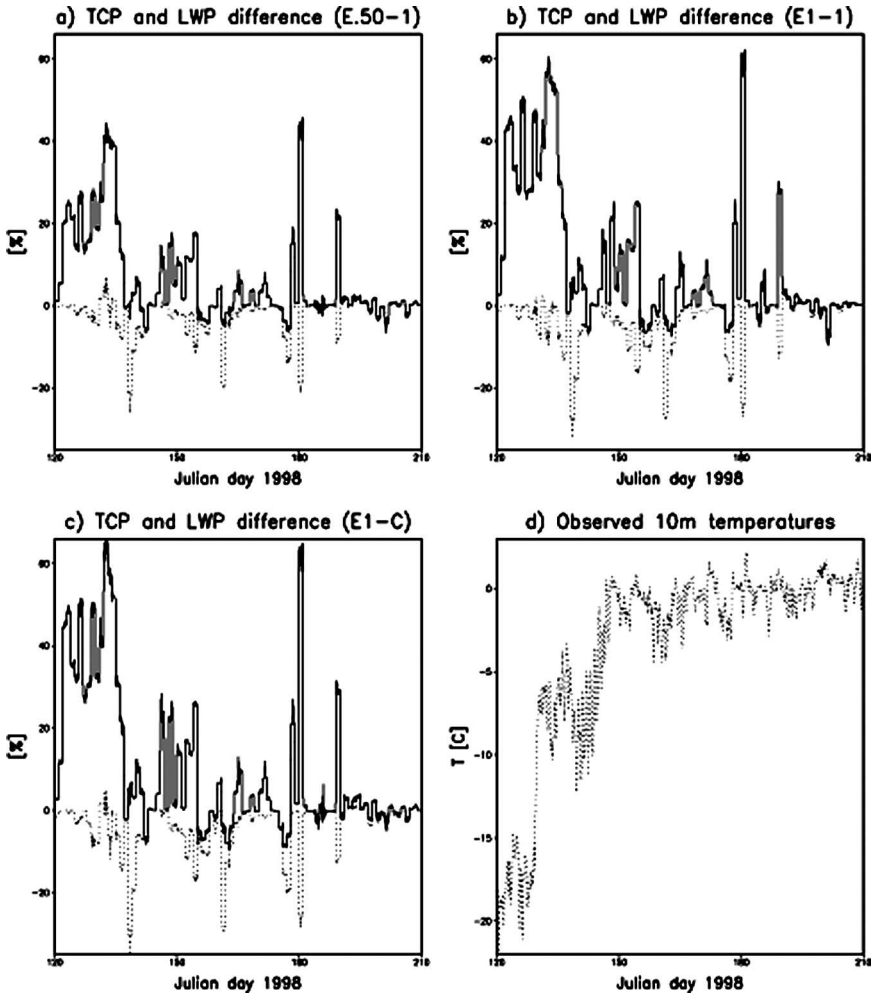

FIG. 4. Comparison of total condensate path (TCP) and LWP simulated values for runs E.50-1, E.75-1, E1-1, and E1-C. Solid and dashed lines denote TCP and LWP percent differences with respect to the control run.

tion of all solid species for the experiments that only differ in the IFN concentrations nudged above the inversion (EC-1, E.50-1, E.75-1, and E1-1). Not surprising, the frequency of occurrence of large values of N_i monotonically increases with higher IFN concentrations within the upper layer. A larger number of ice particles reduces the individual growth by vapor deposition, the aggregation kernels, and the size of the precipitating particles as it can be seen in Fig. 3b. This figure compares the PDFs of the mean mass diameter of the precipitating species (D_i) that in RAMS are categorized as snow and aggregates. The modal diameter of the precipitating ice particles exhibits a clearly monotonic behavior, with lower values for higher IFN concentrations above the inversion. Smaller precipitating particles are naturally associated with lower free-fall speeds and higher residence time, explaining the higher frequency of large IWP values.

Sensitivity experiments also indicate that IFN entrainment from above the inversion produces lower cloud droplet number concentrations (not shown) and significantly lower cloud liquid fractions. Figures 4a–c compare the total condensate path (which includes all hydrometeors; TCP) and liquid water path (LWP) simulated for runs E.50-1, E1-1, and E1-C with those of the control run. The observed temperature at 10 m is plotted in Fig. 4d. Percent differences in TCP (solid lines) are positive, indicating TCP values higher than those of the control run. Conversely, negative differences indicate lower LWP values (dashed lines) for these runs. TCP differences are larger for runs in which higher IFN concentrations are assumed within the upper layer. Entrainment of IFN from above the inversion resulted in higher IWP, and larger TCP values at the expense of LWP, significantly reducing liquid water fraction of the clouds. During a period of approxi-

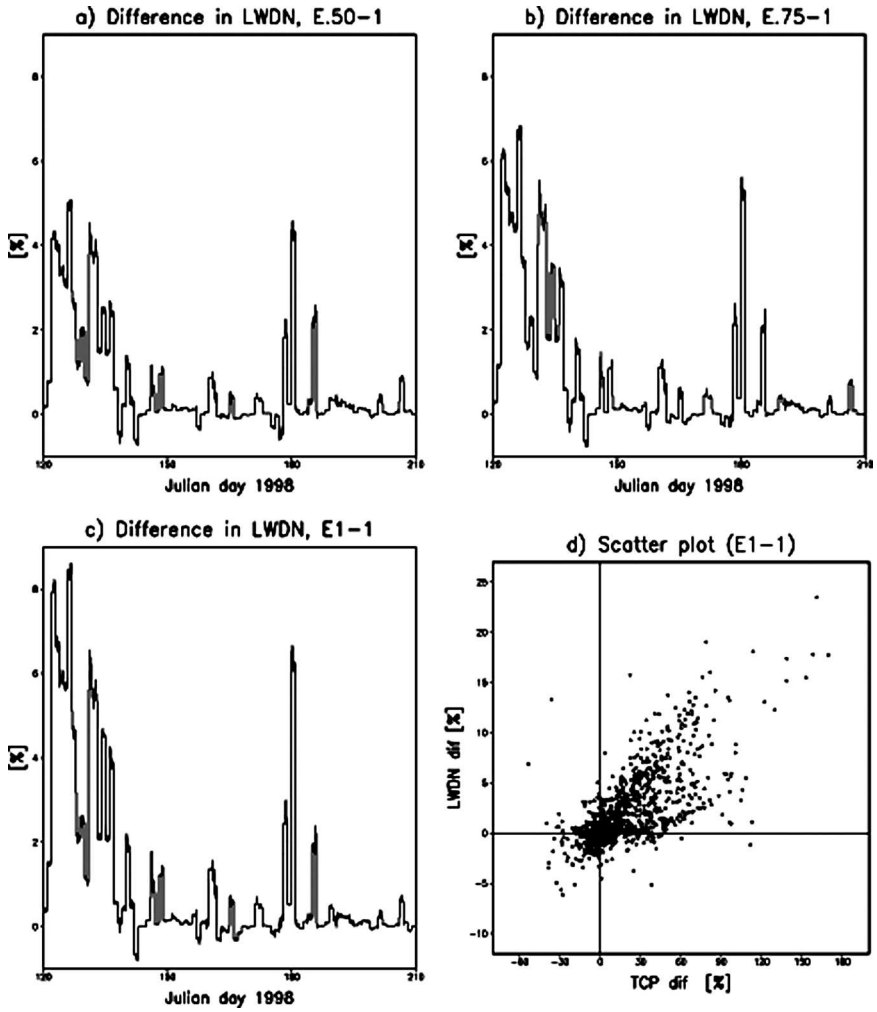

FIG. 5. Percentage differences in the longwave downwelling flux at the surface with respect to the control case for (a) E.50-1, (b) E.75-1, (c) E1-1, and (d) E1-C. Scatterplot relating LWDN and TCP changes.

mately twenty days at the beginning of the simulations, TCP differences are persistently large for all sensitivity runs. The impact of entrained aerosol was more important for these days, the coldest of the simulation period (see Fig. 4d). The largest differences with respect to the control run correspond to the run E1-C (Fig. 4c). The comparison between runs E1-C and E1-1 indicates an opposite although less important effect for CCN entrainment, decreasing TCP and increasing LWP.

The temporal evolutions of LWDN, SWDN, and net radiative forcing (NETRAD) are compared for runs E.50-1, E.75-1, and E1-1 in Figs. 5, 6, and 7, respectively. These percent differences with respect to the control run have been computed using 6-h averages of horizontal mean values. The magnitude of the differences in Figs. 5, 6, and 7 indicates that LWDN, SWDN, and NETRAD vary in a monotonic manner when nudged IFN concentration increase from clean to 50%, 75%, and 100% of the observed values. Again, the largest and most persistent differences closely correspond to the coldest days of the simulation period. When comparing experiment E1-1 with the control run for this period of approximately 20 days, NETRAD on in average 7.1 W m^{-2} higher, corresponding to a LWDN increase of 8.5 W m^{-2}, and a decrease of SWDN (absorbed) of 1.4 W m^{-2}. Scatterplots of LWDN, SWDN, and NETRAD differences against those corresponding to TCP are given in Figs. 5d, 6d, and 7d, respectively. These plots have been generated with hourly model outputs corresponding to the experiment that considers an upper layer with IFN and CCN concentrations consistent with 4 May observations (E1-1). These scatterplots reveal an important degree of association between the changes in radiative fluxes and TCP differences in-

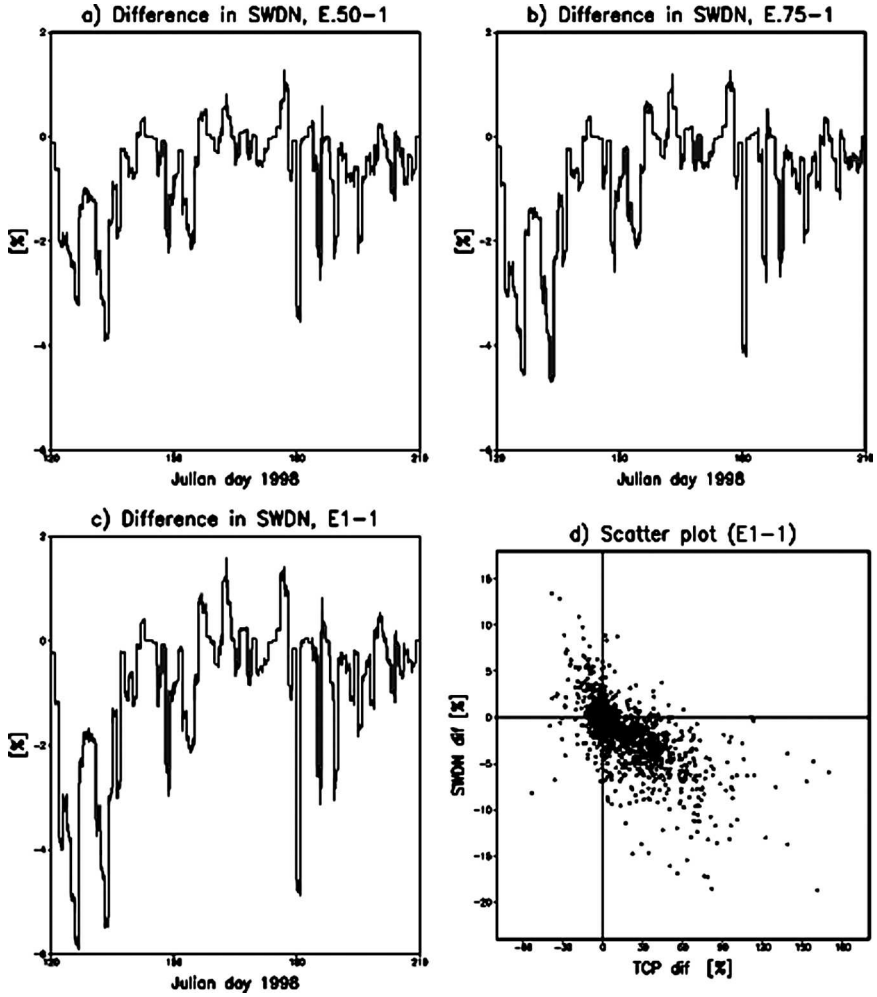

FIG. 6. Same as in Fig. 5, but for shortwave downwelling flux.

duced by the entrainment of IFN. However, lower values of SWDN in the sensitivity runs are physically associated with (optically thinner) clouds with lower LWPs (cf. with Fig. 4). Similar numerical experiments have been performed for a CCN concentration 50% higher, although the main results of Figs. 5, 6, and 7 remained unaltered. Even when positive differences of LWDN (and NETRAD) prevail during the first 60 days of the simulation, small negative differences are found. In most cases, they are associated with a cloud liquid fraction close to unity and tend to prevail during the last 30 days (see Fig. 9b).

In Fig. 8, the simulated evolution of the mean ice thickness for run EC-C is compared with the average of observed values from various gauge stations close to the SHEBA site. The ice thickness was evaluated as a domain average of the areal means of each subgrid ice thickness distribution. Simulated evolution of the snow depth exhibited the same behavior observed at the various gauge stations (not shown). No significant change during May, followed by a rapid decrease, and melted away completely by the end of June (see Sturm et al. 2002). Simulated snow depth reaches zero at approximately Julian day 180 for all numerical experiments. The absence on a snow cover has an important impact on the surface energy exchange; simulated (and observed) melting rates significantly increase because of the abrupt decrease of surface albedo.

The differences in the simulated sea ice thickness with respect to the control run (EC-C) are plotted in Fig. 9b for runs EC-1, E.5-1, E.5-C, E1-1, and E1-C. The cloud liquid fraction, evaluated as the ratio between the liquid water path and TCP of all vertical columns of the domain is given in Fig. 9b for the control

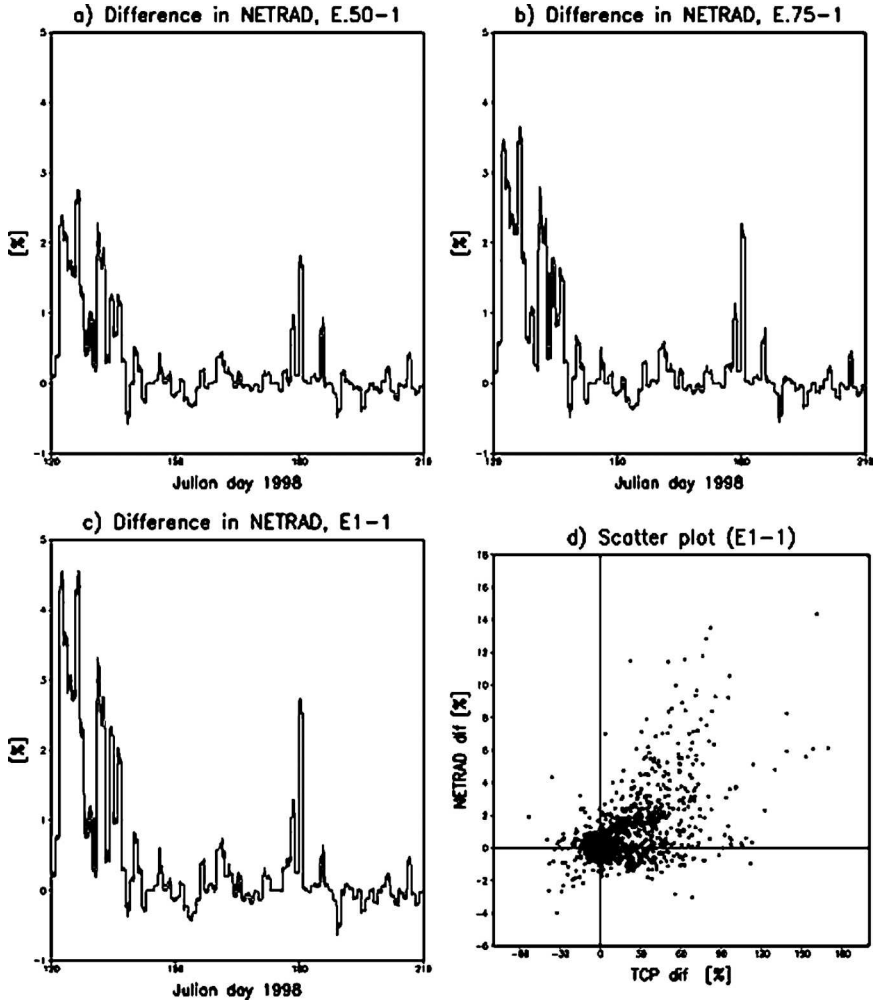

FIG. 7. Same as in Fig. 5, but for the NETRAD.

run. Differences in Fig. 9a are negative for all experiments that consider enhanced IFN concentrations above the inversion, indicating larger melting rates compared to the control case. The largest (negative) differences correspond to the run that considers an upper layer with an IFN concentration consistent with the observations and a clean CCN profile (E1-C). Conversely, larger melting rates were obtained for run EC-1 that only takes into account CCN entrainment. The sign and the magnitude of these differences indicate that the CCN influence is opposite but less important than that associated with IFN entrainment. Simulated sea ice melting rates resulted higher when enhanced IFN concentrations were assumed within the upper layer increase. This behavior is independent of the nudging profile assumed for CCN as can be seen by comparing E.50-C and E.50-1 with E1-C and E1-1, respectively. If we compare run E1-1 and E1-C, it can be seen that slightly lower melting rates were obtained for the experiment that considers an enhanced CCN concentration above the boundary layer. An analogous comparison can be made between runs E.5-1, and E.5-C. Finally, it can be seen that the effect of CCN entrainment is negligible unless the clouds are predominantly liquid as typically occur later in the spring.

5. Summary

In this study we evaluated the potential effects of enhanced aerosol concentrations above the inversion on sea ice melting rates and the surface energy budget. For this study, the Los Alamos National Laboratory sea ice model was implemented into RAMS. Additionally, the coupled model was used with a sophisticated microphysical package that, among other new features, takes into account the nucleation of cloud droplets

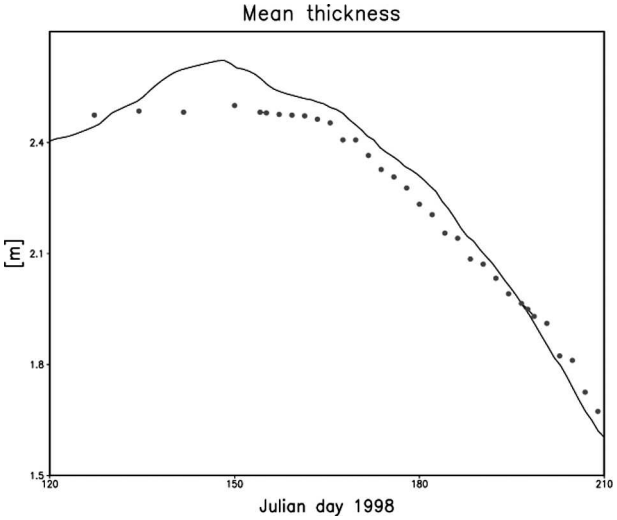

FIG. 8. Comparison of the mean ice thickness simulated for the control run with observations. Solid lines and dots denote simulated and observed values, respectively.

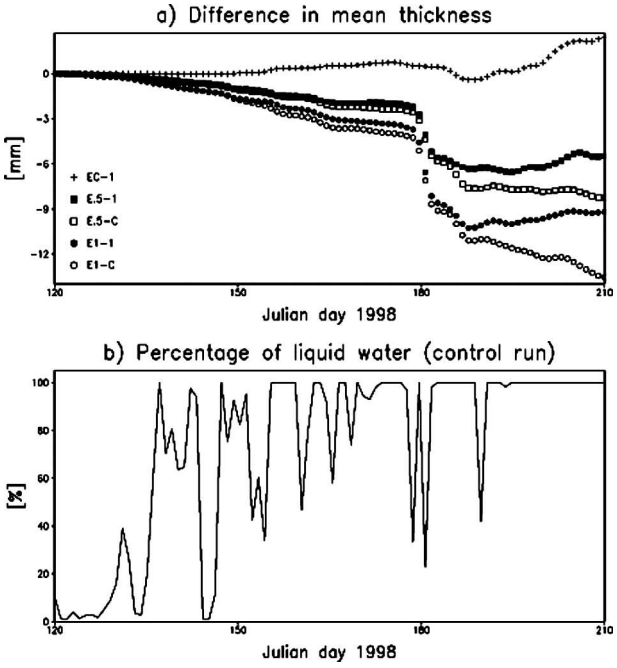

FIG. 9. (a) Comparison of the mean ice thickness simulated for the control run with observations. Solid lines and dots denote simulated and observed values, respectively. (b) Comparison of ice thickness evolutions corresponding to runs EC-1, E.5-1, E.5-C, E1-1, and E1-C. Curves in (b) represent differences with respect to the control run.

avoiding the limiting constrains of selecting a cloud droplet mean diameter.

We performed seven cloud-resolving simulations for the spring–summer period from 1 May to 31 July 1998. In one experiment we assumed clean CCN and IFN concentrations while in the remaining six we considered the intrusion of air masses polluted to various degrees in terms of IFN and CCN concentrations above the boundary layer. Airborne aerosol data corresponding to 4 May 1998 (FIRE/SHEBA field) were used as benchmarks for the design of these experiments. These multimonth simulations have been performed using 2–3 daily SHEBA soundings nudged into the cloud-resolving model to represent daily variations in the synoptic atmosphere.

Our major results of the present paper are consistent with those of Part I that examined the mixed-phase boundary layer cloud case of 4 May 1998. However, important differences were noted for time periods in which only liquid phase clouds were present. For all runs, mixed-phase clouds prevailed during the first two months of simulation. Conversely, clouds with very high liquid fractions were simulated during the last month.

The effects of IFN entrainment while mixed-phase clouds are present can be summarized as follows: LWP decreases while TCP increases due to an important increase in the IWP. The probability density functions obtained for the entire period indicate higher frequencies for large total number concentrations of ice particles and lower modal sizes for precipitating ice categories. Consequently, IFN entrainment reduces the free-fall speed of snow crystals and aggregates, and precipitation rates (see also Part I). Therefore, the important increase in IWP is associated with the longer residence times of the ice particles. Surface radiative fluxes are also affected, LWDN increases and a reduction of lesser magnitude was simulated for SWDN, resulting in larger values of NETRAD. The changes in the radiative fluxes caused by IFN entrainment exhibit an important degree of association with those of TCP. Sea ice melting rates were larger than those of the control run for all experiments that considered IFN entrainment. On the one hand, it must be noted that all integrated water paths, PDFs, radiative fluxes, as well as the sea ice melting rates exhibited a clearly monotonic behavior when increasing IFN concentrations were assumed to characterize the polluted upper layer. On the other hand, these results showed a low sensitivity to the CCN concentration within the upper layer.

Changes of the opposite sign in surface fluxes were simulated for short time periods when high liquid fraction clouds were present, and during the last month. The entrainment of CCN tends to decrease NETRAD and reduce the melting rates with respect to the experiments that consider the same IFN concentrations and clean CCN profile above the inversion. The effects of

CCN entrainment are small when mixed-phase clouds prevail. However they become more important during the last month. The effect on melting rates associated with the presence of enhanced CCN concentrations above the boundary layer is opposite although less important than that of IFN entrainment.

In summary, our results suggest that the entrainment of a polluted air layer overriding the inversion enhances sea ice melting rates. Melting rates were approximately 4% higher than those of the control run while mixed-phase clouds prevailed (the first two months). As mentioned in section 3, clean concentrations are also nudged within the boundary layer for all experiments to efficiently isolate the effect of entrained aerosols from above the inversion. We must await daily observations of IFN and CCN profiles before we can determine the total impacts of aerosol intrusions into the Arctic on climate. While such intrusions are episodic, we can expect that on some occasions the concentrations of cloud nucleating aerosols will be much greater than found on 4 May 1998. The results suggested by these multimonth CRM simulations may have important climatological implications since the extent and duration of sea ice coverage not only affects regional climate but also global climate through ice-albedo feedbacks.

Future work will concentrate on performing similar studies for the freezing (fall) season and, also on air intrusions that differentially enhance CCN concentrations with respect to IFN and vice versa. Work underway in our group includes developing methods for inferring CCN and IFN concentrations from satellite data and developing a model that parameterizes source functions of these aerosols and predicting their Lagrange transport and removal.

Acknowledgments. This research was supported by University of Alaska Fairbanks Research Contract UAF-00-0086/FP100092 (CSU 5-33422) and by NSF Grant 0215367. The authors also wish to thank Bill Lipscomb for providing the CICE code and consulting support on its use, Steve Saleeby for useful discussions, and Brenda Thompson for technical support.

REFERENCES

Alexander, M. A., U. S. Bhatt, J. E. Walsh, M. S. Timlin, J. S. Miller, and J. D. Scott, 2004: The atmospheric response to realistic Arctic sea ice anomalies in an AGCM during winter. *J. Climate,* **17,** 890–905.

Carrió, G. G., H. Jiang, and W. R. Cotton, 2005: Impact of aerosol intrusions on the Arctic boundary layer clouds. Part I: 4 May 1998 case. *J. Atmos. Sci.,* **62,** 3082–3093.

Cotton, W. R., and Coauthors, 2003: RAMS 2001: Current status and future directions. *Meteor. Atmos. Phys.,* **82,** 5–29.

Curry, J. A., and E. E. Ebert, 1990: Sensitivity of the thickness of Arctic sea ice to the optical properties of clouds. *Ann. Glaciol.,* **14,** 43–46.

——, and ——, 1992: Annual cycle of radiation fluxes over the Arctic Ocean: Sensitivity to cloud optical properties. *J. Climate,* **5,** 1267–1280.

——, D. Randall, W. B. Rossoe, and J. L. Schramm, 1996: Overview of Arctic cloud and radiation characteristics. *J. Climate,* **9,** 1731–1764.

——, and Coauthors, 2000: FIRE Arctic Clouds Experiment. *Bull. Amer. Meteor. Soc.,* **81,** 5–29.

Feingold, G., B. Stevens, W. R. Cotton, and R. L. Walko, 1994: An explicit cloud microphysical/LES model designed to simulate the Twomey effect. *Atmos. Res.,* **33,** 207–233.

Gregory, D., and D. Morris, 1996: The sensitivity of climate simulations to the specification mixed-phase clouds. *Climate Dyn.,* **12,** 641–651.

Harrington, Y. Y., T. Reisin, W. R. Cotton, and S. M. Kreidenweis, 1999: Cloud resolving simulations of Arctic stratus. Part II: Transition-season clouds. *Atmos. Res.,* **51,** 45–75.

Heintzenberg, J., H.-C. Hansson, J. A. Ogren, D. S. Covet, and J.-P. Blanchet, 1986: Physical and chemical properties of Arctic aerosols and clouds. *Arctic Air Pollution,* B. Stonehouse, Ed., Cambridge University Press, 25–35.

Hunke, E. C., and W. H. Lipscomb, 1999: CICE: The Los Alamos sea-ice model, documentation and software, version 2.0. Los Alamos National Laboratory, LA-CC-98-16, v.2.

Jiang, H., W. R. Cotton, J. O. Pinto, J. A. Curry, and M. J. Weissbluth, 2000: Cloud resolving simulations of mixed-phase Arctic stratus observed during BASE: Sensitivity to concentration of ice crystals and large-scale heat and moisture advection. *J. Atmos. Sci.,* **57,** 2105–2117.

——, G. Feingold, W. R. Cotton, and P. G. Duynkerke, 2001: Large-eddy simulations of entrainment of cloud condensation nuclei into the Arctic boundary layer: May 18, 1998, FIRE/SHEBA case study. *J. Geophys. Res.,* **106,** 15 113–15 122.

Lipscomb, W. H., 2001: Remapping the thickness distribution of sea-ice. *J. Geophys. Res.,* **106,** 13 989–14 000.

Maykut, G. A., and N. Untersteiner, 1971: Some results from a time dependent thermodynamic model of sea ice. *J. Geophys. Res.,* **76,** 1550–1575.

Meyers, M. P., R. L. Walko, J. Y. Harrington, and W. R. Cotton, 1997: New Rams cloud microphysics parameterization: Part II. The two-moment scheme. *Atmos. Res.,* **45,** 3–39.

Mitchell, D. L., A. Macke, and Y. Liu, 1996: Modeling cirrus clouds. Part II: Treatment of radiative properties. *J. Atmos. Sci.,* **53,** 2967–2988.

Olsson, P. Q., and J. Y. Harrington, 2000: Dynamics and energetics of the cloudy boundary layer in simulations of off-ice flow in the marginal ice zone. *J. Geophys. Res.,* **105D,** 11 889–11 899.

——, ——, G. Feingold, W. R. Cotton, and S. M. Kreidenweis, 1998: Exploratory cloud-resolving simulations of boundary-layer Arctic stratus clouds, Part I, Warm-season clouds. *Atmos. Res.,* **47-48,** 573–597.

Perovich, D. K., and Coauthors, 1999: *SHEBA: Snow and Ice Studies.* CD-ROM. [Available from D. Perovich, CRREL, 72 Lyme Road, Hanover, NH 03755.]

Pielke, R. A., and Coauthors, 1992: A comprehensive meteorological modeling system—RAMS. *Meteor. Atmos. Phys.,* **49,** 69–91.

Ritter, B., and J. F. Geleyn, 1992: A comprehensive radiation scheme for numerical weather prediction models with poten-

tial applications in climate simulations. *Mon. Wea. Rev.,* **120,** 303–325.

Rogers, D. C., P. J. DeMott, and S. M. Kreidenweis, 2001: Airborne measurements of tropospheric ice-nucleating aerosol particles in the Arctic spring. *J. Geophys. Res.,* **106,** 15 053–15 063.

Royer, J. F., S. Planton, and M. Deque, 1990: A sensitivity experiment for the removal of Arctic sea ice with the French spectral general circulation model. *Climate Dyn.,* **5,** 1–17.

Saleeby, S. M., and W. R. Cotton, 2004: A large-droplet model and prognostic number concentration of cloud droplets in the Colorado State University Regional Atmospheric Modeling System (RAMS). Part. I: Module descriptions and supercell test simulations. *J. Appl. Meteor.,* **43,** 182–195.

Shaw, G. E., 1986: Aerosol in the Arctic air masses. *J. Atmos. Chem.,* **4,** 157–171.

Slingo, A., and M. Schreckner, 1982: On shortwave properties of stratiform water clouds. *Quart. J. Roy. Meteor. Soc.,* **108,** 407–426.

Sturm, M., J. Holmgren, and D. K. Perovich, 2002: Winter snow cover on the sea ice of the Arctic Ocean at the Surface Heat Budget of the Arctic Ocean (SHEBA): Temporal evolution and spatial variability. *J. Geophys. Res.,* **107,** 8047, doi:10.1029/2000JC000400.

Yum, S. S., and J. G. Hudson, 2001: Vertical distributions of cloud condensation nuclei spectra over the springtime Arctic Ocean. *J. Geophys. Res.,* **106,** 15 045–15 052.